

Proceedings of the 31st
Risø International Symposium on Materials Science:
*Challenges in materials science and possibilities
in 3D and 4D characterization techniques*
Editors: N. Hansen, D. Juul Jensen,
S.F. Nielsen, H.F. Poulsen and B. Ralph
Risø National Laboratory for Sustainable Energy,
Technical University of Denmark, 2010

ENGINEERING RELATED NEUTRON DIFFRACTION
MEASUREMENTS PROBING STRAINS, TEXTURE AND
MICROSTRUCTURE

Bjørn Clausen[†], Donald W. Brown[‡], Carlos N. Tomé[‡],
Levente Balogh[‡] and Sven C. Vogel[†]

[†]LANSCE-LC, [‡]MST-8
Los Alamos National Laboratory, Los Alamos, NM 87545, USA

ABSTRACT

Neutron diffraction has been used for engineering applications for nearly three decades. The basis of the technique is powder diffraction following Bragg's Law. The measured diffraction patterns provide information about internal strains, texture and microstructure, which can be deduced from the peak positions, peak intensities, and peak widths, respectively. Most structural materials are anisotropic on the grain level and thus the effects of intergranular strains must be considered, and combining the neutron diffraction measurements with polycrystal deformation modeling has proven invaluable in determining the overall stress and strain values of interest in designing and dimensioning engineering components. Furthermore, the combined use of diffraction measurements and polycrystal deformation modeling has provided a unique tool for elucidating basic material properties, such as critical resolved shear stresses for the active deformation modes and their evolution as a function of applied deformation.

1. INTRODUCTION

The penetration depth of neutrons is on the order of centimeters for many common structural metals, such as steel, aluminum, nickel, magnesium and titanium, and thus in combination with gauge volumes in the range of 1-1000 mm³, they provide a true bulk measurement of the behavior of materials without having to deal with surface specific conditions. The deep penetration facilitates the use of advanced sample environment for in-situ type measurements as it is easy to design load frames, furnaces, cryogenic chambers, etc., that allow for neutron access. There are two main categories of engineering related neutron diffraction measurements; spatially resolved measurements, and in-situ measurements. The former addresses the variation of stress as a function of location within a component, such as stresses due to forming (Webster

1994) and diffusion welding (Winholtz and Krawitz 1995; Bouchard et al. 2005), friction stir welding (Staron et al. 2002), thermal stresses in composites (Fitzpatrick et al. 1995; Daymond and Withers 1996), and changes in stresses during a components life cycle (Holden et al. 1988; Jun et al. 2009). In these types of measurements the results have been used to refine and validate numerical calculations, such as finite element model (FEM) calculations (Saigal et al. 1993; Richards et al. 2007), and as it is a non-destructive technique, the diffraction measurements have been used to validate other residual stress measurements techniques, e.g. hole drilling (Yazdi et al. 1998; Stefanescu et al. 2003) and contour method (Zhang et al. 2004; Pagliaro et al. 2009) as multiple techniques can be applied to the same sample. The latter category, in-situ measurements, is mainly aimed at determining the mechanical behavior and micromechanics of advanced materials under conditions that approximate the processing or operation conditions of engineering materials, such as superalloys in jet turbines (Ma et al. 2008), shape memory alloys in low temperature actuators (Krishnan et al. 2008) and piezo-electric actuators (Jones et al. 2007). Furthermore, performing spatially resolved measurements during processing, such as friction stir welding (Woo et al. 2007), can provide detailed information about the transient material behavior.

In the present work, we will focus on the coupling of in-situ neutron diffraction measurements and polycrystal deformation modeling, how the evolution of the experimental techniques has driven the development of the models, and vice versa. The in-situ loading measurements provide direct information about the internal strains within a material as a function of e.g. applied load (Allen et al. 1992), temperature (Choo et al. 1999), magnetic field (Glavatska et al. 2003; Molnar et al. 2008), or combinations thereof (Daymond et al. 1999). This paper will describe the coupled recent advances in experimental and self-consistent polycrystal deformation models that have resulted in higher fidelity between the two. The elastic-plastic self-consistent (EPSC) model has successfully been used to investigate high symmetry materials, such as aluminum (Pang et al., 2000) and stainless steel (Clausen et al. 1999), where dislocation glide is the main deformation mode. Historically, the experiments and models have been connected by the determination and calculation of the internal strains, at the grain level. More recently, the inclusion of grain rotations and stress relaxation associated with deformation twinning (Clausen et al. 2008) has allowed for modeling of a new class of materials, i.e. low symmetry materials that lack sufficient slip systems for accommodating arbitrary deformation, and as a result, twin proficiently. Neil et al. (Neil et al. 2010) expanded the EPSC model framework to a large strain formulation, including the kinematics of large strains and rigid rotations, and the evolution of texture and grain shape due to large scale plasticity. The predicted texture changes due to twinning and large scale plasticity can be compared directly with neutron diffraction measurements providing a second level of critical comparison between model and experiment. Finally, a dislocation based hardening law has been introduced into the self-consistent models to make the constitutive law more physically based, as opposed to empirical. The predicted development of dislocation densities can be directly compared to measured dislocation densities determined from peak width and peak profile changes. Thus we see that as either deformation characteristics or the materials themselves have become more complicated, both the experimental and modeling techniques have evolved to provide additional layers of comparison. Examples experiments related to each of these model developments will be presented.

2. NEUTRON DIFFRACTION MEASUREMENTS

The basis for strain measurement via diffraction is the interatomic spacing within the grains comprising the crystalline material; the lattice plane spacing is used as an internal strain gauge and thus the technique provides strain information on the length scale of the grains. In general

there are two categories of neutron sources; monochromatic sources, such as a nuclear reactor, and polychromatic sources, such as a spallation source, see e.g. (Wenk 2006). In both cases the lattice spacing, d_{hkl} , is determined from Bragg's law;

$$\lambda = 2d_{hkl} \sin \theta_{hkl}, \quad (1)$$

where λ is the wavelength and θ_{hkl} is the scattering angle for the reflection given by the Miller indices hkl . At a constant flux source, such as a nuclear reactor, the wavelength of neutrons selected by a monochromator crystal is constant and the scattering angle is scanned to reveal the interatomic spacing, see e.g. (Clausen and Lorentzen 1997). In contrast, at a polychromatic source, it is the scattering geometry which is fixed and the wavelength is scanned to determine the lattice spacing, see e.g. (Wang et al. 2002). Although both techniques can provide the same information, there are subtle but important differences that should be discussed. The time averaged neutron flux at a given wavelength at a reactor source is generally much higher than at a spallation neutron source, which means that one can measure a single diffraction peak faster at a reactor source. However, to measure multiple peaks at a reactor it is necessary to change the scattering geometry (θ - 2θ scans are necessary to measure multiple reflections in the same sample direction) which is a relatively slow process. In general the count time for a given gauge volume is larger at a polychromatic source, but contrary to the monochromatic technique, the time-of-flight (TOF) technique utilized at polychromatic sources enables measurement of a full diffraction pattern in each measurement (typically a 1.5-3.5 Å d-spacing range, depending on the instrument). One further advantage of the TOF technique is that the scattering vectors for all the peaks in the pattern are parallel. This means that all the strains determined from the peaks are in the same direction, and the intensities of the peaks can directly be represented in an inverse pole figure, and likewise, strains can be represented as an inverse strain pole figure (Brown et al. 2003; Wang et al. 2007).

Following Hutchings et al. (Hutchings 2005), the total stress in a polycrystal can be described by stresses on three length scales; Type I, II and III stresses, representing the macro, intergranular and intragranular stresses, respectively. The peak shifts measured by diffraction are influenced by both Type I and II stresses, but not the Type III stresses. The Type III stresses arise from defects within the lattice and non-uniform stresses within the grain, and they do influence the peak width and shape, as discussed later. For all diffraction based strain measurements, the lattice strain, ε^{hkl} , is determined by the change in the measured lattice plane spacing, d^{hkl} , with respect to an assumed stress-free standard;

$$\varepsilon_{hkl} = \frac{\Delta d_{hkl}}{d_0^{hkl}} = \frac{d_{hkl} - d_0^{hkl}}{d_0^{hkl}} = \frac{d_{hkl}}{d_0^{hkl}} - 1, \quad (2)$$

where hkl are the Miller indices for the given diffraction peak. Inherently, the lattice strains measured by diffraction are elastic in nature as they originate in the change in separation of the lattice planes, and plastic deformation is accommodated by mechanisms not affecting the atomic spacing, such as slip and twinning. Hence, the strain measurement does not provide any direct information about plastic strain incurred by the sample. However, it should be noted that the measured elastic strains are directly proportional to the stress in the grains, which can often be related to the specific active plastic deformation modes. Furthermore, the measured lattice strain is directional, i.e. it is measured along the lattice plane normal that coincide with the scattering vector, and it is an average over all the grains contributing to the specific diffraction peak. Hence, the diffraction technique is probing unique sub-sets of grains within the polycrystal related to each other by a common crystallographic orientation relative to the diffraction vector

defined by the instrument, and thus it is well suited to determination of intergranular stresses, or Type II stresses as defined above. This, on one hand, makes it non-trivial to relate the measured lattice strains to the bulk macroscopic residual stresses that are generally of interest to the structural engineer, and on the other hand it makes diffraction a great tool to investigate the micromechanics of deformation.

One of the main sources of intergranular strains is the inherent elastic and plastic anisotropy exhibited by most materials on the grain level. The single crystal elastic constants of even cubic materials are anisotropic, to varying degrees. In the plastic regime, the anisotropy is dictated by the availability of deformation modes and their crystallographic characteristics. High symmetry materials generally have only one or a few deformation modes, such as the $\{111\}(110)$ slip system in FCC materials. Due to the high multiplicity, there are many systems for each mode, and effectively, the plastic anisotropy is relatively low. In contrast, low symmetry materials have multiple active deformation modes (HCP zirconium may have 4 or 5), but due to the low multiplicity each mode provides fewer systems. As some deformation modes are hard to activate, the plastic anisotropy for low symmetry materials is generally higher than for high symmetry materials. As described earlier, the strains measured by diffraction are highly influenced by intergranular strains, and obtaining representative macroscopic strains from the measured lattice strains is not trivial as discussed in detail by Daymond (Daymond 2004). The best approximation to a macroscopic average strain is a texture and stiffness weighted average of all available peaks, but in general the lattice parameters determined by Rietveld full pattern analysis also provides an acceptable average. The Rietveld analysis (Rietveld 1969) is based upon fitting a calculated diffraction pattern to the measured diffraction pattern, where the former is determined from a crystallographic model that takes into account pertinent material properties, such as space group, atom positions, structure factors, thermal parameters, texture, etc. However, as pointed out by Daymond (Daymond 2004), the crystallographic model in the Rietveld refinement does not include any elastic stiffness terms and thus it does not produce a rigorously correct lattice parameter average appropriate for determining the average strain in all cases.

Texture determination. Texture information can readily be extracted from the diffraction data via the measured peak intensities. For full texture analysis, i.e. full orientation distribution function (ODF) determination, without assuming any symmetry in the measured texture, multiple diffraction peaks in multiple directions must be measured. At a monochromatic source, this is typically achieved directly by measuring pole figures for a minimum of three crystallographic reflections, while the sample is rotated around two axes in a goniometer to access the needed real space coverage. Contrary to the strain measurements, it is not crucial that all the diffraction peaks are measured in the same direction with respect to the sample, and thus one-dimensional curved detectors can be used to measure multiple peaks simultaneously, see e.g. (Benmarouane et al. 2005). At a polychromatic source with fixed detectors, many diffraction peaks are recorded simultaneously with collinear diffraction vectors. In other words, at a polychromatic source, the *inverse* pole figure is measured directly, i.e. reciprocal space is heavily sampled. This reduces the necessary real space coverage (sample re-orientation) in the determination of the ODF, simplifying the use of ancillary equipment and allowing for various in-situ texture determination, such as stress (Hartig et al. 2006) and temperature (Lonardelli et al. 2007). For the HIPPO instrument at Los Alamos Neutron Science Center (LANSCE) only four sample rotations about one axis are needed for sufficient pole figure coverage (Wenk et al. 2003). In most cases, when multiple peaks are recorded in one diffraction pattern, Rietveld refinement is the preferred method of determining the ODF from the measured data, utilizing either spherical harmonics or the WIMV method (Matthies et al. 1998), as implemented in the software packages GSAS (Von Dreele 1997) and MAUD (Lutterotti et al. 1997), respectively.

For a more detailed introduction to methods related to texture analysis, see e.g. (Wenk 2006).

Microstructure determination. In diffraction measurements, the peak width and the peak shape is influenced by the microstructure, i.e. intragranular heterogeneities, of the sample. Peak profile analysis is common to laboratory X-ray and synchrotron X-ray measurements where the high angular resolution enables determination of dislocation densities and crystallite size. Earlier work was based solely upon peak widths (Warren and Averbach 1950; 1952; Williamson and Hall 1953; Wilkens 1970), where more recent methods are based upon diffraction line profile analysis and full pattern analysis, e.g. (Ungár and Borbély 1996), and even allowing for determination of densities of multiple dislocation types and twin boundary density (Balogh et al. 2009). Most engineering specific neutron diffraction instruments have a much lower angular resolution (Ungár et al. 2010) and thus peak profile studies are less common (Lukáš et al. 2009; Woo et al. 2009), but are increasing.

3. POLYCRYSTAL DEFORMATION MODELING

For the last decade and a half polycrystal deformation modeling has been used to interpret diffraction data (Pang et al. 1998; Clausen et al. 1999; Agnew et al. 2003), and to provide further insight into the material behavior, accomplished by refining the material properties in the model while fitting the model calculations to the measured diffraction data. There are many types of polycrystal deformation models, but the most common are elastic-plastic self-consistent (EPSC), visco-plastic self-consistent (VPSC) and crystal plasticity finite element modeling (CPFEM). In all the models, the material behavior is described on the grain level by the single crystal elastic and plastic properties, which depend on the crystal structure of the material. Due to the inherent anisotropy of most crystalline materials on the grain level, it is paramount that the models allow for full elastic and plastic anisotropy. The two main differences between the models are the constitutive model used and the assumption of the interaction between grains. For the CPFEM, the grain interactions are taken care of directly within the finite element framework (Dawson 2000) and typically an elasto-viscoplastic constitutive formulation is utilized to describe the plastic behavior (Marin and Dawson 1998). Results from such CPFEM models have been correlated with diffraction measurements for single phase materials, e.g. (Dawson et al. 2001; Loge et al. 2002), and composites, e.g. (Han and Dawson 2005). The CPFEM based models are capable of providing local information about neighboring grains and within grains, and thus they have also been used in combination with synchrotron X-ray measurements of direct grain-to-grain interactions, see e.g. (Lienert 2004; Miller et al. 2008). However, the CPFEM calculations are rather computationally expensive, requiring the use of parallel computing and multiple CPU clusters.

Within the self-consistent models the interaction between the grains is described via mean field approximations, specifically the case of an ellipsoidal inclusion within a homogeneous matrix (Eshelby 1957). The rate independent self-consistent formulation is the EPSC model, first implemented by Hutchinson (Hutchinson 1970) for isotropic materials, and expanded to full anisotropy by Turner and Tomé (Turner and Tomé 1994). This model utilizes a small strain formulation and excludes lattice rotations, so it is applicable to the elastic-plastic transition region and early plasticity only. However, as a part of the model, the full stress and strain tensors are determined for each grain, and by extracting elastic strain averages over grains based upon their orientation, it is possible to directly compare calculated elastic strains with the measured lattice strains from diffraction data. The rate dependent self-consistent model is the VPSC model, see e.g. (Lebensohn and Tomé 1993). It is a true plastic model that does not include elasticity, and thus it is not capable of predicting internal strains for comparison with diffraction measurements. However, it does calculate texture evolution, and has proven to be an

excellent tool to investigate materials behavior and texture development, see e.g. (Blumenthal et al. 2004; Proust et al. 2007; Beyerlein et al. 2007). Recently, elasto-viscoplastic self-consistent (EVPSC) models has been developed, e.g. (Mareau and Daymond 2010; Wang et al. 2010), and since this type of model does include elasticity, it is capable of predicting lattice strains as the EPSC model. The results of the EVPCS model are very comparable to the large strain EPSC model, with slight variations for some reflections.

In the following we will concentrate on the coupling of engineering neutron diffraction measurement and EPSC model calculations and how they have been developed and expanded so that it now is able to compare measured and calculated lattice strain, texture and microstructure data provided.

4. NEUTRON DIFFRACTION AND EPSC MODELING

In-situ neutron diffraction measurements, such as performing a tensile test and neutron diffraction measurements simultaneously, provides the ability to measure the lattice strains as a function of the applied stress. By aligning the loading direction with the scattering vector, the evolution of each individual diffraction peak is representative of the response of that specific subset of grains with a unique plane normal aligned with the loading direction. In the EPSC model, the polycrystal is regarded as an agglomerate of grains of different orientations, and it is possible to extract elastic strains from the subset of grains that present a given lattice plane normal along the loading direction. Hence, a direct comparison between the measured lattice strains and the calculated elastic strains for the grain subsets can be made. This is what has been exploited in the coupled application of neutron diffraction measurements and EPSC modeling. Initially, only the lattice strains were utilized, but the development of both the experimental technique, including data analysis and mining, and the model have been intimately linked. In the following we will describe how the capabilities of the EPSC model has evolved over the last few years, mainly driven by the experimental neutron diffraction work and the desire to make the model more physical and less empirical. Along the way, the neutron diffraction data has served as a guide for development and as a validation tool for the model, and once validated, the EPSC model has been able to provide insights into the underlying micromechanical response of the materials investigated. This is achieved by fitting the model response to the available measured data by refining the material parameters on the grain level, such as the critical resolved shear stresses (CRSS) and hardening behavior. In this sense, the model is used to solve an inverse problem, and hence, it is paramount to use as much measured data as possible to constrain the model fit within the parameter space to ensure the uniqueness of the solution.

Classical EPSC. The ‘classical’ EPSC model as proposed by Hill (Hill 1965) and later implemented by Hutchinson (Hutchinson 1970) and expanded by Turner and Tomé (Turner and Tomé 1994) to account for general elastic and plastic anisotropy, is inherently a small strain model, which means that it does not include kinematics of large strains or rigid rotations. In some implementations (Clausen et al. 1998, 1999; Jia et al. 2008), lattice spins due to slip were accounted for independently, without making them part of the constitutive equations, still leaving it a small strain formulation. This limits the applicable range of deformation for which the model can be used. As long as the deformations and lattice rotations are small the model is a good approximation, which means the elastic region, the elastic-plastic transition region and the early plasticity region. For most single phase metals this corresponds to the first 5-10 % deformation, with cubic materials such as aluminum, copper and steel having the largest range (Clausen et al., 1998, 1999; Daymond et al., 2000; Pang et al., 2000; Lorentzen et al., 2002; Larsson et al., 2004), and lower symmetry materials, such as magnesium, zirconium and beryllium, applicable over a smaller range (Brown et al., 2003; Gharghoury et al., 1999; Agnew

et al., 2003; Clausen et al., 2008; Pang et al., 1999). The cubic materials typically have ample slip systems available and a minimum of twinning activity, which limits the lattice rotation, whereas the lower symmetry materials typically have a limited number of active slip systems and significant amount of twinning activity, which tend to lead to significant texture development even after less than 10% deformation.

The model has been described in detail elsewhere (Hutchinson 1970; Turner and Tomé 1994; Clausen et al. 1998), and we will present only a summary of an example study of uniaxial tension in stainless steel coupling neutron diffraction and EPSC modeling, see (Clausen et al. 1999). Fig. 1a) shows the measured and calculated macroscopic stress-strain curve for stainless steel loaded in uniaxial tension. The neutron diffraction measurements were performed using the NPD instrument at LANSCE utilizing the TOF technique. The model calculation has been fit to the measured macroscopic stress-strain curve using the four Voce hardening parameters, τ_0^s , τ_1^s , θ_0^s and θ_1^s (Larsson et al. 2004), for the {111}(110) slip deformation mode. Fig 1b-c) show the measured and calculated elastic strains parallel to the straining direction for the first 8 unique FCC reflections.

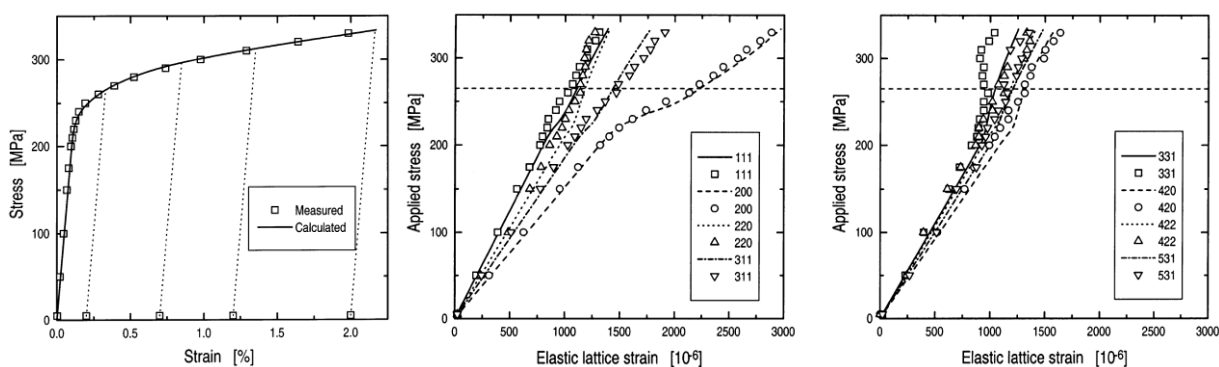


Fig. 1. Measured and calculated macroscopic stress strain curve and lattice strains parallel to the loading axis for stainless steel loaded in uniaxial tension. Symbols are measured data and lines are model data. From (Clausen et al. 1999).

In the elastic region, the elastic strains respond linearly with stress, although the slope or modulus is strongly dependent on the crystal orientation with respect to the loading direction. The EPSC model is able to reproduce the strong anisotropy observed in the elastic region with the 111 reflection being the stiffest and the 200 reflection being the softest. This can only be achieved by including the full anisotropy of the grains and the homogeneous equivalent medium (HEM) representing the polycrystal. Once yielding commences, at about 200 MPa, the lattice response becomes non-linear with applied stress, and some of the reflections, such as 220 and 420, exhibit a steeper slope, whereas other, such as the 111 and the 200, exhibit a shallower slope. This shows that the former are plastically deforming, as their elastic strain no longer increases as much as before for a given stress increment. And *vice versa*, the latter reflections have to carry the load shed by of the plastically deforming reflections, and thus their elastic strain increases more for a given stress increment. Once all grains are plastically deforming, at about 250 MPa another inflection is observed for the 200 reflection, which is the last reflection to go plastic. This is the typical load transfer seen for most polycrystals primarily deforming by slip (Wong and Dawson 2010). As seen in Fig. 1, the EPSC model is capable of reproducing the complex nonlinearity of the reflections through the elastic-plastic transition region and into the early stage of plasticity.

Texture development. As a material undergoes significant plastic deformation it will develop

texture, or preferred crystallographic orientation, caused by grain rotation due to dislocation generation (Bunge 1969). One limitation of the small strain EPSC model is that it does not include such lattice rotation. Recently, this has been addressed to include the lattice reorientation and stress relaxation due to twinning (Clausen et al. 2008), and finally a full large strain formulation was presented by Neil et al. (Neil et al. 2010), including the kinematics of large strains and rigid rotations, and the evolution of texture and grain shape. In the following we will present two examples illustrating how the model improvements enable the use of more of the available neutron diffraction data, namely texture information, to constrain the model fits to the measured data.

The first example addresses the issue of twinning within low symmetry materials, such as magnesium. Full details are given in (Clausen et al. 2008), and here we will only present a short introduction. Magnesium exhibits a high propensity for twinning, employing the $\{10\bar{1}2\}\langle\bar{1}011\rangle$ tensile twin system (Yoo 1981). The tensile twinning is activated when the c-axis of the HCP crystal structure is subjected to tension, and it results in a near 90 degree rotation of the c-axis between the parent and the twin (Brown et al. 2005).

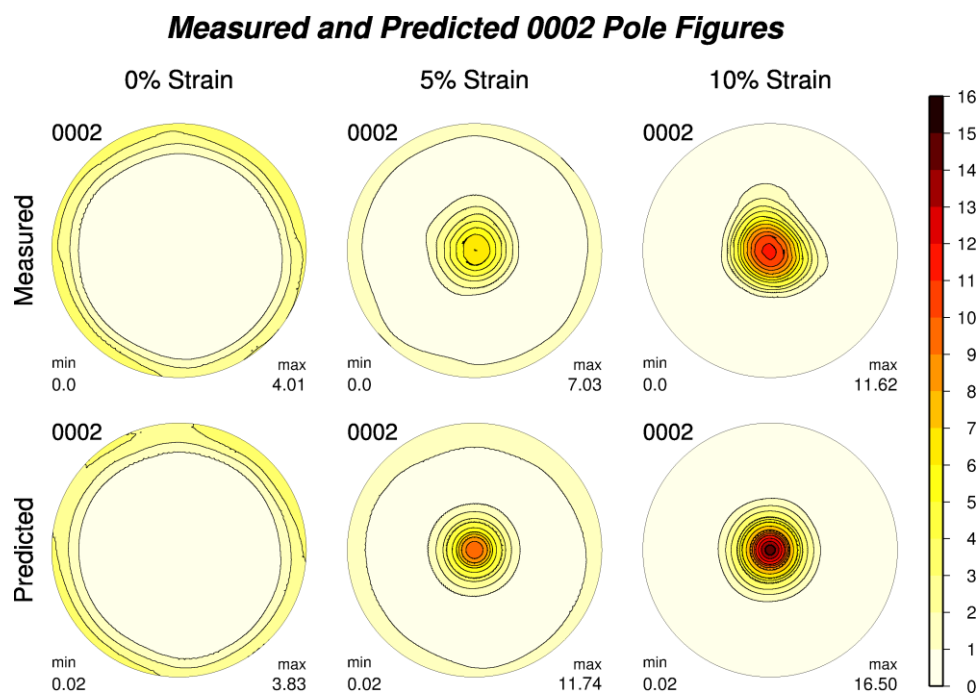


Fig. 2. Measured and predicted basal pole figures for the extruded magnesium alloy loaded in compression. From (Clausen et al. 2008).

The starting material was extruded AZ31B magnesium alloy, which exhibits the so-called ‘rod texture’, where the basal poles of most grains are oriented at an angle of nearly 90 degrees to the extrusion direction, see the initial basal pole figure in Fig. 2. Hence, when loaded in compression along the prior extrusion direction, most of the grains will be subjected to tension along the c-axis, via the Poisson’s strains, favoring twinning as an active deformation mode. As twinning takes place, the intensity increases at the center of the basal pole figure, and it is important to note that as there initially are no grains with their basal lattice plane normal along the loading direction all the grains contributing to the basal peak are twins. The in-situ neutron diffraction measurements were performed using the SMARTS instrument at LANSCE (Bourke et al. 2002). The measured macroscopic stress strain curve and the longitudinal lattice strains are shown in Fig 3. The plateau and sigmoidal shape of the stress-strain curve is indicative of twinning, and as seen Fig. 3b), it is accompanied by a significant redistribution of the internal

strains. It is not possible to reproduce either of these effects using the classical EPSC model described above, which was the driver for developing the twinning scheme presented in (Clausen et al. 2008).

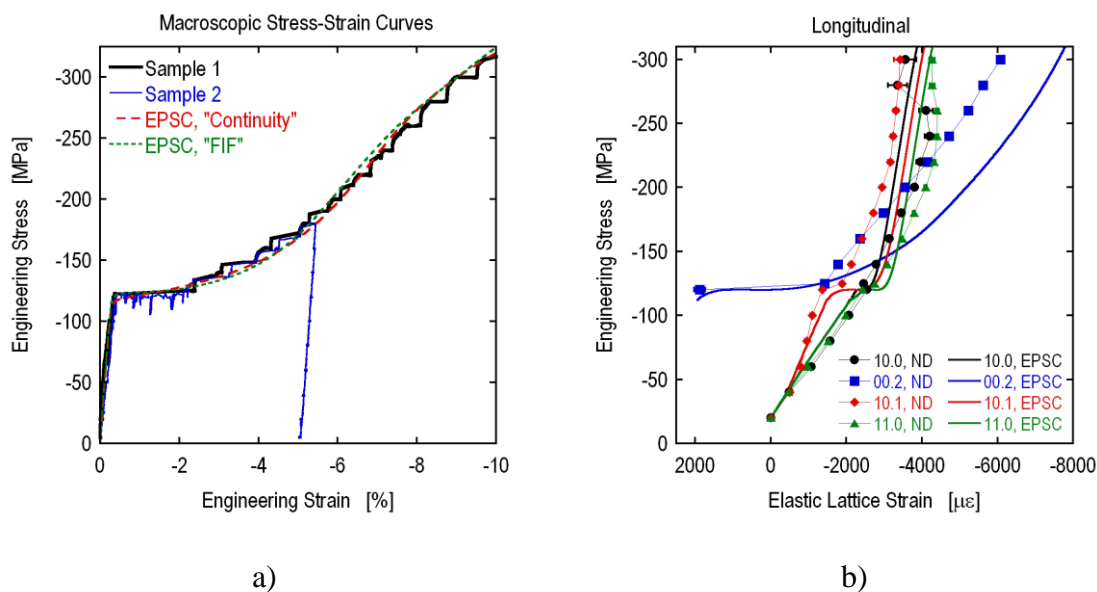


Fig. 3. (a) Measured and predicted macroscopic stress strain curves, and (b) twin volume fraction, for compression of extruded magnesium alloy AZ31B.. From (Clausen et al. 2008).

Within the new twinning formalism, a new grain is generated for each active twin system in the parent grains. The twin grows in size according the amount of accumulated shear on the twin system in the parent grain, but there is no direct interaction between the twin and its parent; the twin is just another grain in the polycrystal. The transfer of volume fraction from the parent grain to the twin(s) generates a change in texture, but the constitutive model is still a small strain formulation. Accounting for the twin formation and growth, via the generation of new grains, allowed the evolution of macroscopic stress, texture and twin volume fraction with strain to be predicted correctly, which could not be accomplished with previous models, see Fig. 2 and 3a). The texture predicted by the model is somewhat sharper than the measured texture, which has been reported as a general situation for texture predictions using the VPSC model as well (Neil et al. 2010) However, accounting for the texture evolution associated with twinning alone is not sufficient for a satisfactory prediction of the internal stress evolution. Specifically, the load reversal observed in the incipient twins (shown in figure 3b) could not be captured. For this reason, it was hypothesized that twin creation is associated with an instability of the system caused by a rapid decrease in stored elastic energy. This process is accompanied by an excess twin shear upon twin nucleation and a sharp local stress reversal in the parent and twin. Hence, stress relaxation was introduced in a rather *ad hoc* manner, in which it is assumed that the twins has a fixed minimum size as they form, called the Fixed Initial Fraction, or FIF in (Clausen et al. 2008). Fig. 4a) shows a schematic of the localized shear within a grain due to formation of a twin and Fig. 4b) shows the reaction forces generated by the surroundings on the parent and twin as the grain shape is changed. Within the FIF formulation, it is assumed that the surroundings force the small twinned portion of the grain back into its original shape (i.e. the grain must fit into the surrounding matrix), and thus generate an elastic back-stress within the twin equal in magnitude, but opposite in sign, to the plastic shear necessary to generate the required minimum twin fraction. For the parent grain, this is implemented by a correction to the stress in the parent in the step where the twin forms generating a stress relaxation determined

from the back-stress in the twin, weighted by the initial twin volume fraction.

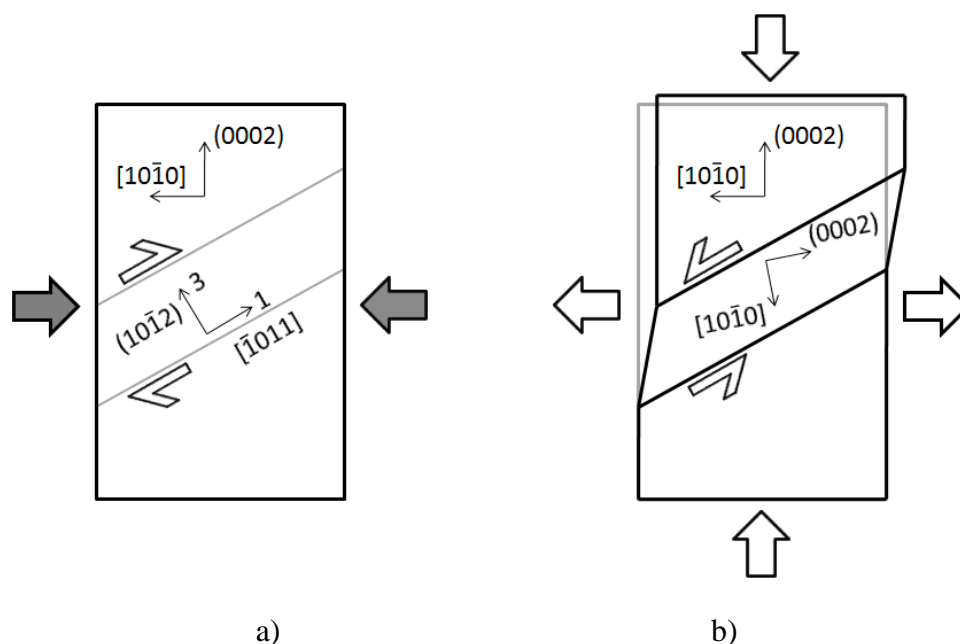


Fig. 4. (a) Schematic of a typical grain in extruded Mg showing the crystallographic elements, the compression direction (shaded arrows), and the resolved shear on the twin plane. (b) Schematic of the tensile twin domain and the medium-induced reaction stresses (arrows) associated with activating a ‘FIF’. A ‘tensile’ reaction component perpendicular to the page (not drawn) is also present. From (Clausen et al. 2008).

For the example of compressive loading of extruded magnesium alloy AZ31B presented here, a FIF of 3% was found to reproduce the stress reversal observed in the newly formed twins. This is consistent with the optimum twin nuclei size found by Zhang et al. (Zhang et al. 2008) using a FEM approach. As seen in Fig. 3b), the model is able to reproduce the measured longitudinal lattice strains, including the sign reversal for the newly formed twins.

As mentioned above, the updated twinning scheme did not change the fact that the EPSC model is a small strain formulation. However, very recently, Neil et al. implemented an EPSC formulation including the kinematics of large strains, rigid body rotations, texture evolution due to dislocation generation and grain shape evolution. Again, we are not going into the details of the model implementation as it is presented elsewhere (Neil et al. 2010), however, it is noteworthy that accounting for the material state at arbitrary strains requires the use of the Jaumann derivative of the Cauchy stress rate as the crystal lattice in the grains will spin with respect to the laboratory and aggregate frames. The example presented here uses the same stainless steel presented earlier in this paper, but this time loaded to 30% true tensile strain as shown in Fig. 5a). The comparison of the measured and calculated lattice strains is shown in Fig. 5b), and it is seen that the large strain model is in good agreement with the measured data, for more details see (Neil et al. 2010). A direct consequence of the texture development is seen for the 220 reflection which disappears at a stress of about 700 MPa. It is because all the grains have rotated away from this orientation, and thus there are no grains over which to determine the strain average. The loading direction is about 60 degrees away from the prior rolling direction. This off-symmetry loading axis serves as a good test of the model with respect to the anisotropy of the HEM representing the polycrystal. The measured and calculated textures after 30% true tension are shown in Fig. 6. The model accurately reproduces the measured texture evolution, including the remaining asymmetry caused by the off-symmetry loading direction. Similar to the

twinning model, the texture prediction is slightly stronger than observed, which also is the case for texture predictions using the VPSC model (Neil et al. 2010).

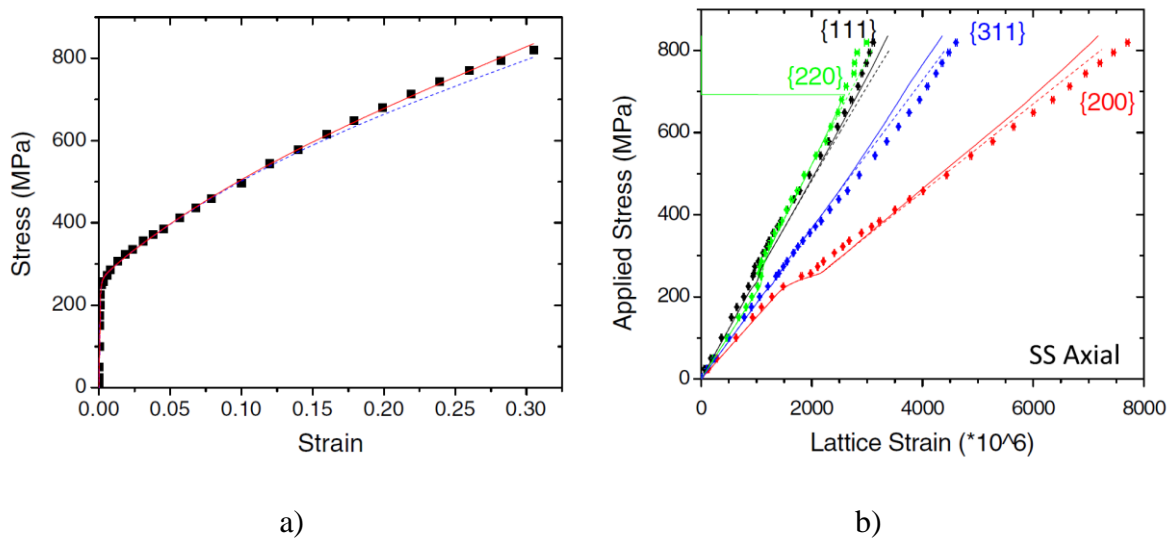


Fig. 5. Measured and predicted macroscopic stress-strain curves (a), and longitudinal lattice strains (b). Symbols are neutron diffraction measurements, lines are model predictions (solid and dashed lines are for the large and small strain models, respectively). From (Neil et al. 2010).

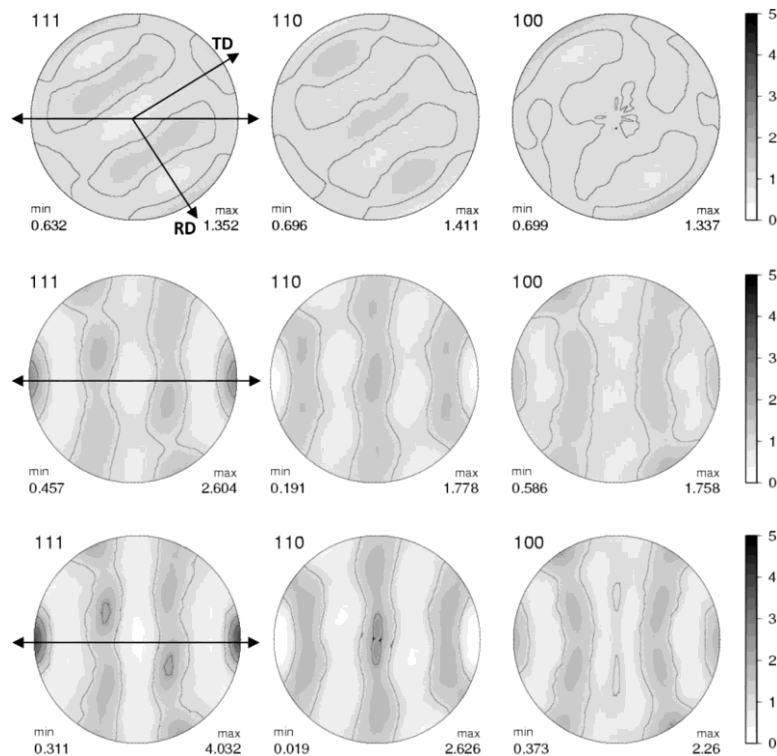


Fig. 6. Measured and calculated pole figures for the stainless steel; measured initial texture (top), measured final texture (middle), and calculated final texture (bottom). Note the remaining asymmetry at 30% true strain caused by the initial rolling texture. From (Neil et al. 2008).

Dislocation based hardening law. The developments to the EPSC model described above have enabled the use of texture data from the diffraction measurements to be included when constraining the model calculations. The last bit of information from the diffraction data that up until now has not been utilized to guide the development of the model is the peak width evolution which can provide information about the microstructure, e.g. the dislocation densities and grain sizes. A major corner-stone of the EPSC model, and the underlying Eshelby inclusion theory (Eshelby 1957), is that the stress and strain within a grain is uniform. Hence, the intragranular effects, the Type III stresses, that causes the peak width changes in the diffraction data cannot be directly included into the EPSC framework. Recently, Beyerlein and Tomé presented a hardening law based upon the development of the stored dislocation density for a VPSC model (Beyerlein and Tomé 2008).

In the following, we will present a summary of a preliminary adaptation of this stored dislocation density based hardening scheme for the EPSC model. In their original formulation for the VPSC model, the stored dislocation densities were referred to the active deformation modes, but in the following we have expanded that to describing the stored dislocation density development on individual systems within the modes. The evolution law for the stored dislocation density is based upon one of the most widely used thermal activation models by Essmann and Mughrabi (Essmann and Mughrabi 1979) which was further developed by Mecking and Kocks (Mecking and Kocks 1981; Kocks and Mecking 2003);

$$\frac{\partial \rho^\alpha}{\partial \gamma^\alpha} = \frac{\partial \rho_{storage}^\alpha}{\partial \gamma^\alpha} - \frac{\partial \rho_{removed}^\alpha}{\partial \gamma^\alpha} = k_1^\alpha \sqrt{\rho^\alpha} - k_2^\alpha \rho^\alpha, \quad (3)$$

featuring competing storage and removal terms for the dislocation density, ρ^α , with respect to the shear, γ^α , on each system α . In the model used in the current analysis, Beyerlein and Tomé (Beyerlein and Tomé 2008) account for two dislocation populations; the total stored dislocations, ρ^α , and the dislocations locked in sub-structure within the grains, ρ_{sub} . The later is represented by a grain average in the model, and it is found from the removal term presented in Eq. 3 by splitting the removed dislocation into a part that is being annihilated and a part that is locked into the sub-structure;

$$\frac{\partial \rho_{removed}^\alpha}{\partial \gamma^\alpha} = (1 - f^\alpha) \frac{\partial \rho_{removed}^\alpha}{\partial \gamma^\alpha} + f^\alpha \frac{\partial \rho_{removed}^\alpha}{\partial \gamma^\alpha} = \frac{\partial \rho_{ann.}^\alpha}{\partial \gamma^\alpha} + \frac{\partial \rho_{sub}}{\partial \gamma^\alpha}, \quad (4)$$

where the latter term is found as;

$$\frac{\partial \rho_{sub}}{\partial \gamma^\alpha} = q A^\alpha b^\alpha \sqrt{\rho_{sub}} k_2^\alpha \rho^\alpha. \quad (5)$$

A^α is a temperature dependent term that describes the fractional rate of dislocations that generate sub-structure (it incorporates the f^α term in Eq. 4), and q is the rate coefficient which reflects how debris can grow from point defects seeded by the local thermal-activated reactions. The ratio of the pre-factors for the storage and removal terms in the dislocation evolution law (Eq. 3), k_1^α and k_2^α , is expressed as follows;

$$\frac{k_2^\alpha}{k_1^\alpha} = \frac{\chi b^\alpha}{g^\alpha} \left(1 - \frac{kT}{D^\alpha (b^\alpha)^3} \ln \left(\frac{\dot{\epsilon}}{\dot{\epsilon}_0} \right) \right), \quad (6)$$

where χ is a dislocation interaction coefficient, b^α is the Burgers vector, g^α is a normalized stress-independent activation energy, D^α is a drag term with unit of stress, and $\dot{\epsilon}_0$ is a reference strain rate, see (Beyerlein and Tomé 2008) for details. Work hardening is linked to the evolution of stored dislocations, their mutual interactions, and their interactions with barriers in the microstructure. In the model, the CRSS for each slip system, τ_c^α , includes contributions from forest dislocations and sub-structure in addition to the initial value, τ_0^α ;

$$\tau_c^\alpha = \tau_0^\alpha + \tau_{for}^\alpha + \tau_{sub}^\alpha, \quad (7)$$

where

$$\tau_{for}^\alpha = b^\alpha \chi \mu^\alpha \sqrt{\rho^\alpha} \quad \text{and} \quad \tau_{sub}^\alpha = -k_{sub} \mu^\alpha b^\alpha \sqrt{\rho_{sub}} \ln(b^\alpha \sqrt{\rho_{sub}}). \quad (8)$$

k_{sub} is a material-independent constant determined to be 0.086 (Madec et al., 2002), and μ^α is the directional shear modulus on the slip plane in the direction of the Burgers vector. The hardening of the twin systems is dealt with separately as there is no provision for self-hardening for the twin systems;

$$\tau_{twin}^\beta = \tau_0^\beta + \mu^\beta \sum_{\alpha} C^{\beta\alpha} b^\beta b^\alpha \rho^\alpha, \quad (9)$$

where $C^{\alpha\beta}$ is an interaction matrix, describing the hardening of the twin systems by the slip systems. The choice of not providing self hardening on twin systems is consistent with the results for the twinning scheme presented earlier, where it was assumed that the twin systems did not harden at all. The same example used for the large strain implementation above, uniaxial loading of stainless steel to 30% true strain in tension, is presented here again, but this time using the preliminary dislocation based hardening model.

Table 1. Parameters for the dislocation based hardening law.

Parameter	Value
A^α	70
k_1^α	2.75×10^8
g^α	3.8×10^{-3}
D^α	300 MPa
τ_0^α	87 MPa
χ	0.35
$\rho^{\alpha,ini}$	5.0×10^9
ρ_{sub}^{ini}	1.0×10^{11}
b^α	2.546×10^{-10}
$\dot{\epsilon}_0$	10^7
$\dot{\epsilon}$	10^{-5}
q	4

The parameters in the dislocation based hardening law have been used to fit the model

calculations to the measured data, which in this case means; A^α in Eq. 5, k_1^α , g^α and D^α in Eq. 6 and τ_0^α from Eq. 7. The dislocation interaction coefficient, χ from Eq. 6, was set to 0.35, which is appropriate for FCC metals (Madec et al. 2002). The other parameters, given in Table 1, are left at default values, see (Beyerlein and Tomé 2008).

The measured and calculated macroscopic stress-strain curves and the longitudinal lattice strains are shown in Fig. 7. The agreement between dislocation based model and measurement for the macro strain and the lattice strains is nearly as good as for the large strain EPSC model with Voce hardening law presented in Fig. 5, but the predicted macro curve is slightly more linear at higher strains where the measured curve has a decreasing slope, and the 311 reflection deviates more severely from the measured behavior. This gives a first indication that the preliminary stored dislocation density based hardening law does not capture all the underlying physics. The predicted texture after 30% true uniaxial strain is very similar to the one predicted by the Voce hardening model, see Fig. 6.

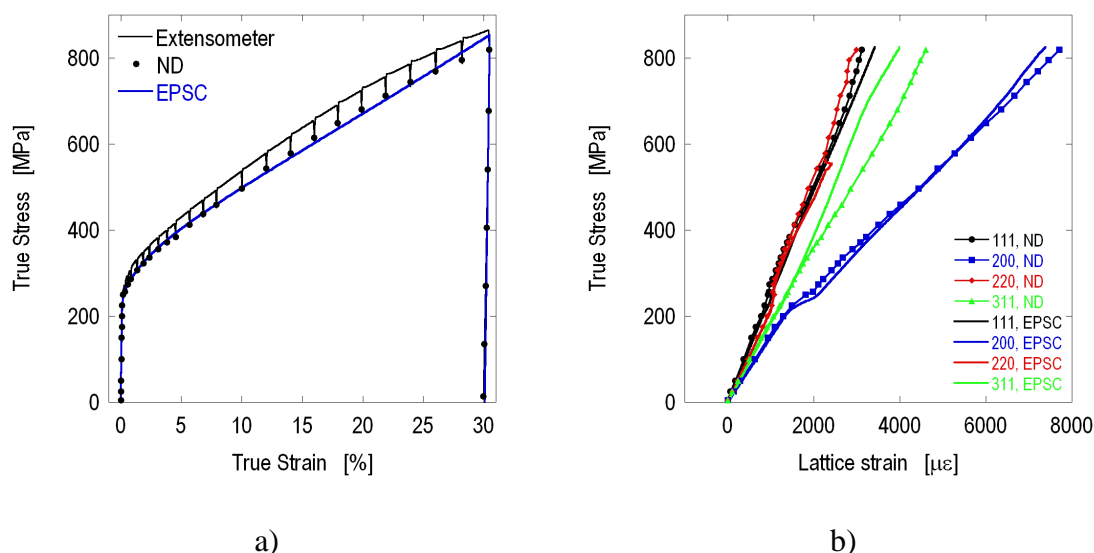


Fig. 7. Measured and calculated macroscopic stress-strain curve (a) and (b) longitudinal lattice strains for stainless steel loaded in uniaxial tension to 30% true strain. Symbols are neutron diffraction measurements, lines are model predictions.

The total dislocation density and area-weighted mean subgrain size was determined from the diffraction data taken during the uniaxial loading of stainless steel to 30% true strain discussed above. This preliminary analysis was done using the convolutional multiple whole profile (CMWP) method (Ungár et al. 2001; Ribárik et al. 2004, Balogh et al. 2008), in which the measured intensity profiles are fitted by theoretical functions calculated on the basis of a model of the microstructure. It is important to note that the dislocation density determined by diffraction methods is the *total* dislocation density, whereas the hardening model presented above is based upon the *stored* dislocation density, which is a subset of the total dislocation density (Kocks et al. 1975).

The analysis requires a precise measurement of the instrumental profile for the given sample dimensions which was not available. Hence, the diffraction pattern measured at zero stress was used as the instrumental pattern, meaning that any prior dislocation density in the sample would skew the results. However, the samples were cut from an annealed plate, and the initial dislocation density should be minimal. The dislocation densities determined from the diffraction

patterns, Fig. 8a), increase approximately linearly with strain, to a maximum value of about $42 \times 10^{14} \text{ m}^{-2}$. This value is relatively high compared to a published value of $8 \times 10^{14} \text{ m}^{-2}$ for copper deformed in compression to 70% true strain (Balogh et al. 2006). The subgrain size, Fig. 8b), could not be refined below 10% strain, but at higher strains it shows a decreasing trend to a final value of about 130 nm at 30% strain. The stored dislocation densities, total, forest and substructure, predicted by the EPSC model with the dislocation density based hardening law are presented in Fig. 8c). It is clear that the predicted *stored* dislocation density is only a fraction of the measured *total* dislocation density. The missing part of the equation is the *mobile* dislocation density. According to Kocks et al. (Kocks et al. 1975), the mobile dislocation density can be estimated by

$$\rho_{mobile} = \frac{2}{3} \left(\frac{2\pi\sigma}{\mu b} \right)^2. \quad (10)$$

Using values for the maximum load in the current example, the estimated mobile dislocation density is approximately $140 \times 10^{14} \text{ m}^{-2}$, or about a factor of 3 higher than the measured total dislocation density.

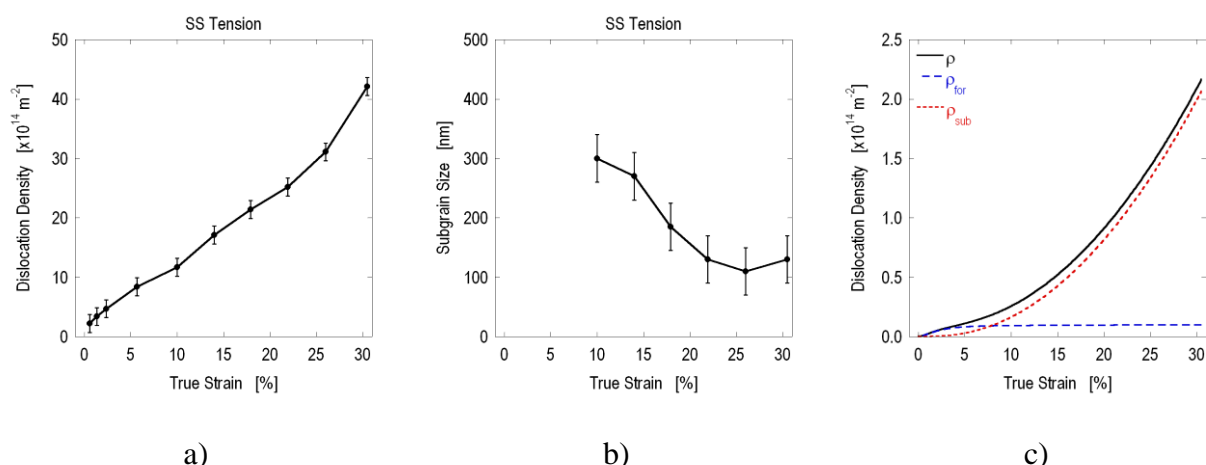


Fig. 8. Measured *total* dislocation density (a) and subgrain size (b) during uniaxial tension of stainless steel to a final true strain of 30%. Calculated *stored* dislocation density using the dislocation density based hardening law (c).

From the above example it is obvious that the preliminary hardening law based upon the stored dislocation density, as presented here, is not practical for direct comparisons with total dislocation densities measured by diffraction. However, the example nicely illustrates the iterative process by which the EPSC model is being developed as driven by advances in experimental techniques and the associated data analysis.

5. SUMMARY AND OUTLOOK

The combined use of neutron diffraction and polycrystal deformation modelling has proven to be an excellent approach to understanding the micromechanics of engineering materials. The non-destructive neutron diffraction measurements allow for true bulk measurements of internal strains in most structural metals, and the models can be used to determine material parameters, such as initial critical resolved shear stress and hardening parameters for the active deformation modes. Once validated, the models become predictive and can be used for materials design. The

neutron diffraction measurements provide information about strain, texture and the microstructure, but up until recently, the EPSC model was only capable of predicting the lattice strains. With development of a physically based twinning scheme (Clausen et al. 2008) and the expansion into the large strain regime (Neil et al. 2010), the model is now able to predict the texture development as well. The large strain EPSC formulation provides a new use of the model by virtue of the fact that it is formulated in the full deformation gradient, and thus it can be applied as a materials model within finite element codes. A combination of EPSC and FEM will enable investigation of problems with heterogeneous Type I stresses, with the ability to predict the spatial variation of internal stress, texture and microstructure. Previously, the VPSC model has been used as a materials model within various FEM codes, e.g. (Engler et al. 2000; Tomé et al. 2001), although only providing the plastic deformation and hence the texture development.

Work is ongoing to develop a dislocation based hardening law into the EPSC model, and preliminary results for uniaxial loading of stainless steel were presented. The basis for the preliminary model is the stored dislocation density, and from the presented example it is clear that further development is needed before the measured and calculated dislocation densities can be directly compared. With a successful implementation of a dislocation based hardening law into the EPSC model it will finally be possible to use all the experimental information available and to formulate the model in physically sound microstructure-based framework.

ACKNOWLEDGEMENTS

All authors, except SCV, were fully supported by the U.S. Department of Energy, Office of Basic Energy Sciences, Division of Materials Sciences and Engineering, Project FWP 06SCPE401 under U.S. DOE Contract No. W-7405-ENG-36. This work has benefited from the use of the Lujan Neutron Scattering Center at LANSCE, which is funded by the Office of Basic Energy Sciences (DOE). Los Alamos National Laboratory is operated by Los Alamos National Security LLC under DOE Contract DE-AC52-06NA25396.

REFERENCES

- Agnew, S.R., Tomé, C.N., Brown, D.W., Holden, T.M. and Vogel, S.C. (2003). *Scripta Mater.*, vol. 48(8), pp. 1003-1008.
- Allen, A.J., Bourke, M.A.M., Dawes, S., Hutchings, M.T. and Withers, P.J. (1992). *Acta Mater.*, vol. 40(9), pp. 2361-2373.
- Balogh, L., Gubicza, J., Hellmig, R.J., Estrin, Y. and Ungár, T. (2006). *Z. Kristallogr., Suppl.* 23, pp. 381-386.
- Balogh, L., Tichy, G. and Ungár, T. (2009). *J. Appl. Cryst.*, vol. 42(4), pp. 580-591.
- Balogh, L., Nauyoks, S., Zerda, T.W., Pantea, C., Stelmakh, S., Palosz, B. and Ungár, T. (2008). *Mat. Sci. Eng. A*, vol. 487(1-2), pp. 180-188.
- Benmarouane, A., Hansen, T., Millet, P. and Lodini, A. (2005). *Solid State Phenomena*, vol. 105, pp. 427-432.
- Beyerlein, I.J., Alexander, D.J. and Tomé, C.N. (2007). *J. Mater. Sci.*, vol. 42(5), pp. 1733-1750.
- Beyerlein, I.J. and Tomé, C.N. (2008). *Int. J. Plas.*, vol. 24(5), pp. 867-895.
- Blumenthal, W.R., Brown, D.W. and Tomé, C.N. (2004). *AIP Conference Proceedings*, vol. 706(1), pp. 525-528.
- Bouchard, P.J., George, D., Santisteban, J.R., Bruno, G., Dutta, M., Edwards, L., Kingston, E. and Smith, D.J. (2005). *Int. J. of Pressure Vessels and Piping*, vol. 82(4), pp. 299-310.
- Bourke, M.A.M., Dunand, D.C. and Ustundag, E. (2002). *Appl. Phys. A*, vol. 74(suppl.2), pp. S1707-S1709.

- Brown, D.W., Bourke, M.A.M., Clausen, B., Holden, T.M., Tomé, C.N. and Varma, R. (2003). *Metall. Mater. Trans. A*, vol. 34(7), pp. 1439-1449.
- Brown, D.W., Agnew, S.R., Bourke, M.A.M., Holden, T.M., Vogel, S.C. and Tomé, C.N. (2005). *Mat. Sci. & Eng. A*, vol. 399(1-2), pp. 1-12.
- Bunge, H.J. (1969), *Mathematische Methoden der Texturanalyse*. Berlin: Akademie Verlag.
- Choo, H., Rangaswamy, P. and Bourke, M.A.M. (1999). *Scripta Mater.*, vol. 42(2), pp. 175-181.
- Clausen, B. and Lorentzen, T. (1997). *Metall. Trans. A*, vol. 28(12), pp. 2537-2541.
- Clausen, B., Lorentzen, T. and Leffers, T., (1998). *Acta Mater.*, vol. 46(9), pp. 3087-3098.
- Clausen, B., Lorentzen, T., Bourke, M.A.M. and Daymond, M.R., (1999). *Mater. Sci. Eng. A*, vol. 259(1), pp. 17-24.
- Clausen, B., Tomé, C.N., Brown, D.W. and Agnew, S.R. (2008). *Acta Mater.*, vol. 56(11), pp. 2456-2468.
- Dawson, P.R. (2000). *International Journal of Solids and Structures*, vol. 37(1-2), pp. 115-130.
- Dawson, P., Boyce, D., MacEwen, S. and Rogge, R. (2001). *Mater. Sci. and Eng. A*, vol. 313(1-2), pp. 123-144.
- Daymond, M.R. and Withers, P.J. (1996). *Scripta Mater.*, vol. 35(6), pp. 717-720.
- Daymond, M.R. (2004). *J. Appl. Phys.*, vol. 96(8), pp. 4263-4272.
- Daymond, M.R., Tomé, C.N. and Bourke, M.A.M. (2000). *Acta Mater.*, vol. 48(2), pp. 553-564.
- Daymond, M.R., Lund, C., Bourke, M.A.M. and Dunand, D.C. (1999). *Metall. Trans. A*, vol. 30(11), pp. 2989-2997.
- Engler, O., Huh, M.-Y. and Tomé, C.N. (2000). *Metall. Trans. A*, vol. 31(9), pp. 2299-315.
- Eshelby, J.D. (1957). *Proc. R. Soc. Lond. A*, vol. 241(1226), pp. 376-396.
- Essmann, U. and Mughrabi, H. (1979). *Phil. Mag. A*, vol. 40(6), 731-756.
- Fitzpatrick, M.E., Hutchings, M.T. and Withers, P.J. (1995). *Physica B*, vol. 213-214, pp. 790-792.
- Gharghoury, M.A., Weatherly, G.C., Embury, J.D. and Root, J. (1999). *Philos. Mag. A*, vol. 79(7), pp. 1671-1695.
- Glavatska, N., Mogilniy, G., Glavatsky, I., Danilkin, S., Hohlwein, D., Beskrovnij, A., Söderberg, O. and Lindroos, V.K. (2003). *J. Phys.*, vol. 112(2), pp. 963-967.
- Han, T.-S. and Dawson, P.R. (2005). *Mater. Sci. and Eng. A*, vol. 405(1-2), pp. 18-33.
- Hartig, C., Vogel, S.C. and Mecking, H. (2006). *Mat. Sci. & Eng. A*, vol. 437(1), pp. 145-150.
- Hill, R. (1965). *J. Mech. Phys. Solids*, vol. 13(2), pp. 89-101.
- Holden, T.M., Root, J.H., Fidleris, V., Holt, R.A. and Roy, G. (1998). *Mat. Sci. Forum*, vol. 27-28, pp. 359-370.
- Hutchings, M.T., Withers, P.J., Holden, T.M. and Lorentzen, T. (2005). *Introduction to the Characterization of Residual Stress by Neutron Diffraction*. Taylor & Francis; New York, pp. 10-16.
- Hutchinson, J.W. (1970). *Proc. R. Soc. Lond. A*, vol. 319, pp. 247-272.
- Jia, N., Lin Peng, R., Wang, Y.D., Johansson, S. and Liaw, P.K. (2008). *Acta Mater.*, vol. 56(4), pp. 782-793.
- Jones, J.L., Pramanick, A., Nino, J.C., Motahari, S.M., Ustundag, E., Mark R. Daymond, M.R. and Oliver, E.C. (2007). *Appl. Phys. Lett.*, vol. 90(17), pp. 172909-1-3.
- Jun, T.-S., Hofmann, F., Belnoue, J., Song, X., Hofmann, M. (2009). *J. Strain Analysis Eng. Design*, (2009), vol. 44(7), pp. 563-568.
- Kocks, U.F, Argon, A.S. and Ashby, M.F. (1975). *Progress in Materials Science*, vol. 19, pp. 1-281.
- Kocks, U.F. and Mecking, H. (2003). *Prog. Mater. Sci.*, vol. 48(3), pp. 171-273.
- Larsson, C., Clausen, B., Holden, T.M. and Bourke, M.A.M. (2004). *Scripta Mater.*, vol. 51(6) , pp. 571-575.
- Lebensohn, R.A. and Tomé, C.N. (1993). *Acta Mater.*, vol. 41(9), pp. 2611-2624.

- Lienert, U., Han, T.-S., Almer, J., Dawson, P.R., Leffers, T., Margulies, L., Nielsen, S.F., Poulsen, H.F. and Schmidt, S. (2004). *Acta Mater.*, vol. 52(15), pp. 4461-4467.
- Loge, R.E., Turkmen, H.S., Miller, M.P., Rogge, R. and Dawson, P.R. (2002). *Materials Science Forum*, vol. 404-407, pp. 69-76.
- Lonardelli, I., Gey, N., Wenk, H.-R., Humbert, M., Vogel, S.C. and Lutterotti, L. (2007). *Acta Mater.*, vol. 55(17), pp. 5718-5727.
- Lorentzen, T., Daymond, M.R., Clausen, B. and Tomé, C.N. (2002). *Acta Mater.*, vol. 50(6), pp. 1627-1638.
- Lukáš, P., Strunz, P., Davydov, V., and Kužel, R. (2009). *Powder Diffraction*, vol. 24(S1), pp. S26-S30.
- Lutterotti, L., Matthies, S., Wenk, H.-R., Schultz, A.J. and Richardson, J.W. (1997). *J. Appl. Phys.*, vol. 81, pp. 594.
- Krishnan, V.B., Manjeri, R.M., Clausen, B., Brown, D.W. and Vaidyanathan, R. (2008). *Mat. Sci. & Eng. A*, vol. 481(SI), pp. 3-10.
- Ma, S., Seetharaman, V. and Majumdar, B.S. (2008). *Acta Mater.*, vol. 56(15), pp. 4102-4113.
- Madec, R., Devincre, B., and Kubin, L.P. (2002). *Phys. Rev. Lett.*, vol. 89(25), pp. 255508/1-255508/4.
- Mareau, C. and Daymond, M.R. (2010). *Acta Mater.*, vol.58(9), pp. 3313-3325.
- Marin, E.B. and Dawson, P.R. (1998). *Comput. Methods Appl. Mech. Engrg.*, vol. 165, pp. 1-21
- Matthies, S., Wenk, H.-R. and Vinel, G.W., (1998). *J. Appl. Cryst.*, vol. 21, pp. 285-304.
- Matthies, S. and Vinel, G.W., (1982). *Phys. Stat. Sol. B*, vol. 112(2), pp. K111-K114.
- Mecking, H. and Kocks, U.F. (1981). *Acta Metall.*, vol. 29(11), pp. 1865-1875.
- Miller, M.P., Park, J.-S., Dawson, P.R. and Han, T.-S. (2008). *Acta Mater.*, vol. 56(15), pp. 3927-3939.
- Molnar, P., Sittner, P., Novak, V., Prokleska, J., Sechovsky, V., Ouladdiaf, B., Hanulla, S.P. and Heczko, O. (2008). *J. Phys. Condens. Matter*, vol. 20(10), pp. 4224-4224.
- Neil, C.J., Wollmershauser, J.A., Clausen, B., Tomé, C.N., and Agnew, S.R. (2010). In press. *Int. J. Plasticity*, doi:10.1016/j.ijplas.2010.03.005
- Pagliari, P., Prime, M.B., Clausen, B., Lovato, M.L. and Zuccarello, B. (2009). *J. Eng. Mater. Tech.*, vol. 131(3), p.031002.
- Pang, J.W.L., Holden, T.M. and Mason, T.E. (1998). *J. Strain Analysis for Engineering Design*, vol. 33(5), pp. 373-384.
- Pang, J.W.L., Holden, T.M., Turner, P.A. and Mason, T.E. (1999). *Acta Mater.*, vol. 47(2), pp. 373-383.
- Pang, J.W.L., Holden, T.M., Wright, J.S. and Mason, T.E. (2000). *Acta Mater.*, vol. 48(5), pp. 1131-1140.
- Proust, G., Tomé, C.N. and Kaschner, G.C. (2007). *Acta Mater.*, vol. 55(6), pp. 2137-48.
- Ribárik, G., Gubicza, J. and Ungár, T. (2004). *Mat. Sci. & Eng. A*, vol. 387-389(2-3), pp. 343-347.
- Richards, D.G., Prangnell, P.B., Withers, P.J., Williams, S.W., Wescott, A. and Oliver, E.C. (2007). *Mat. Sci. Forum*, vol. 539-543(1-5), pp. 4025-4030.
- Rietveld, H.M. (1969). *J. Appl. Cryst.*, vol. 2(2), pp. 65-71.
- Saigal, A., Kupperman, D.S., Singh, J.P., Singh, D., Richardson, J. and Bhatt, R.T. (1993). *Composites Engineering*, vol. 3(11), pp. 1075-1086.
- Staron, P., Kocak, M. and Williams, S. (2002). Residual Stresses in Friction Stir Welded Al Sheets. *Appl. Phys. A*, vol. 74(S2), pp. S1161-2.
- Stefanescu, D., Browne, P., Truman, C.E. and Smith, D.J. (2003). *Mat. Sci. Forum*, vol. 440(4), pp. 85-92.
- Tomé, C.N., Maudlin, P.J., Lebensohn, R.A. and Kaschner, G.C. (2001). *Acta Mater.*, vol. 49(15), pp. 3085-3096.
- Turner, P.A. and Tomé, C.N. (1994). A Study of Residual Stresses in Zircaloy-2 with Rod

- Texture. *Acta Metall.*, vol. 42(12), pp. 4143-4153.
- Ungár, T., Balogh, L. and Ribárik, G. (2010). *Metall. Trans. A.*, vol. 41(5), pp. 1202-1209.
- Ungár, T. and Borbély, A. (1996). *Appl. Phys. Lett.*, vol. 69(21), pp. 3173-3175.
- Ungár, T., Gubicza, J., Ribarik, G. and Borbely, A. (2001). *J. Appl. Cryst.*, vol. 34(3), pp. 298-310.
- Vaidyanathan, R., Bourke, M.A.M. and Dunand, D.C. (1999). *Acta Mater.*, vol. 47(12), pp. 3353-3366.
- VonDreele, R.B. (1997). *J. Appl. Cryst.*, vol. 30(4), pp. 517-525.
- Wang, H., Wu, P.D., Tomé, C.N. and Huang, Y. (2010). *J. Mech. Phys. Solids*, vol. 58(4), pp. 594-612.
- Wang, Y.D., Brown, D.W., Choo, H., Liaw, P.K., Cong, D.Y., Benson, M.L. and Zuo, L. (2007). *Phys. Rev. B*, vol.75(17) 174404.
- Wang, X.L., Wang, Y.D., and Richardson, J.W. (2002). *J. Appl. Cryst.*, vol. 35(5), pp. 533-537.
- Warren, B.E. and Averbach, B.L. (1950). *J. Appl. Phys.*, vol. 21(6), pp. 595-599.
- Warren, B.E. and Averbach, B.L. (1952). *J. Appl. Phys.*, vol. 23(4), pp. 497-497.
- Webster, P.J. (1994). *Steel Times*, vol. 222(5), pp. 182-3.
- Wenk, H.-R. (2006). *Neutron Scattering in Earth Sciences*. Mineralogical Society of America, Chantilly, Va.
- Wenk, H.-R., Lutterotti, L. and Vogel, S. (2003). *Nuclear Inst. Methods in Phys. Res. A*, vol. 515, pp. 575-588.
- Wilkins, M. (1970). *Phys. Status Solidi A*, vol. 2(2), pp. 359-370.
- Williamson, G.K. and Hall, W.H. (1953). *Acta Metall.*, vol. 1, pp. 22-31.
- Winholtz, R.A. and Krawitz, A.D. (1995). *Metall. Trans. A*, vol. 26(5), pp. 1287-1295.
- Woo, W., Feng, Z., Wang, X.L., Brown, D.W., Clausen, B., An K., Choo, H., Hubbard, C.R. and David, S.A. (2007). *Sci. Tech. Welding and Joining*, vol. 12(4), pp. 298-303.
- Woo, W., Ungár, T., Feng, Z.L., Kenik, E. and Clausen, B. (2009). *Metall. Trans. A.*, vol. 41(5), pp. 1210-1216.
- Yazdi, S.R., Reiraint, D. and Lu, J. (1998). *J. Strain Ana. Eng. Des.*, vol. 33(6), pp. 449-458.
- Yoo, M.H., (1981). *Metall. Trans. A*, vol. 12(3), pp. 409-418.
- Zhang, R.Y., Daymond, M.R. and Holt, R.A. (2008). *Mat. Sci. & Eng. A*, vol. 473(1-2), pp. 139-146.
- Zhang, Y., Ganguly, S., Edwards, L. and Fitzpatrick, M.E. (2004). *Acta Mater.*, vol. 52(17), pp. 5225-5232.